



A weak-coupling expansion for viscoelastic fluids applied to dynamic settling of a body

Matthew N.J. Moore^{*}, Michael J. Shelley

Courant Institute, New York University, 251 Mercer Street, New York, NY 10012, United States

ARTICLE INFO

Article history:

Received 12 April 2012

Received in revised form 20 July 2012

Accepted 23 July 2012

Available online 2 August 2012

Keywords:

Oldroyd-B

Boger fluid

Transient velocity overshoot

Weak-coupling

Lagrangian method

Birefringent strand

ABSTRACT

The flow of viscoelastic fluids is an area in which analytical results are difficult to attain, yet can provide invaluable information. We develop a weak-coupling expansion that allows for semi-analytical computations of viscoelastic fluid flows coupled to immersed structures. In our method, a leading-order polymeric stress evolves according to a Newtonian velocity field, and this stress is used to correct the motion of bodies. We apply the method to the transient problem of a sphere settling through a viscoelastic fluid using the Oldroyd-B model, and recover previous results and observed behavior. The theory presented here is in contrast to the retarded-motion, or low-Weissenberg-number, expansions that have seen much application. One advantage of the weak-coupling method is that it offers information for Weissenberg numbers larger than one. The expansion's limit of validity is closely related to the diluteness criterion of a Boger fluid. We extend the classical settling problem to include an oscillatory body-force, and show how the introduction of a second time-scale modifies the body-dynamics.

© 2012 Elsevier B.V. All rights reserved.

1. Introduction

A sphere released from rest in a viscoelastic fluid exhibits a transient velocity overshoot before eventually settling to terminal velocity, as has been established through experiments using Boger fluids [1–4]. This is an attractive benchmark problem for the interaction of viscoelastic fluids with structures due to the simple geometry yet non-trivial flow and stress fields that arise. The complexity of the flow and stress fields makes it a challenge for numerical methods, but gives rise to clearly observable dynamic behavior that can be compared to experiments.

Fig. 1 shows the qualitative transient behavior observed in experiments [1,2,4]. The sphere accelerates from rest and reaches a maximum velocity U_m , before settling to a terminal velocity U_t . The acceleration from rest to U_m is due to inertia (of the body and/or the fluid), which is neglected in the present study. The transient velocity overshoot, on the other-hand, is a viscoelastic phenomenon that does not require inertia. It is due to the development of an extra polymeric stress in the fluid, a macroscopic quantity caused by the stretching of microscopic polymers. The extra polymeric stress is initially isotropic and uniform, implying that it does not contribute to drag. However, as time progresses deformation leads to a non-trivial polymeric stress field, which exerts an additional drag on the body and slows its motion. The

time-scale of the velocity overshoot is most often reported to be comparable to the polymeric relaxation time τ_p , while its relative magnitude $(U_m - U_t)/U_t$ has been estimated by the viscosity ratio η_p/η_s , where η_s is the viscosity of the Newtonian solvent and η_p is the polymeric viscosity [2,4]. An important dimensionless parameter is the Weissenberg number, $Wi = \tau_p V/L$, where V is a characteristic velocity and L is a characteristic length-scale. A second dimensionless parameter must involve the viscosity ratio, and for this we introduce the parameter β defined by the relationship $\beta Wi = \eta_p/\eta_s$. When the problem is non-dimensionalized accordingly (time is scaled by L/V), the qualitative behavior is a velocity overshoot of relative magnitude $(U_m - U_t)/U_t \approx \beta Wi$, occurring on a dimensionless time-scale of order Wi .

Previous theoretical studies fall mainly into two categories: asymptotic calculations that rely on a retarded-motion expansion and numerical simulations of non-linear viscoelastic models. The retarded-motion expansion assumes that the flow time-scale L/V is long compared to τ_p , or $Wi \ll 1$. Linear rheology and the second-order fluid model are two of the simplest results of a retarded-motion expansion. More generally, the expansion of any viscoelastic constitutive model in small Wi fits into this category. Some important studies related to the settling sphere are as follows: Leslie and Tanner calculated the first two terms of a low- Wi expansion to determine the steady-state drag as a function of Wi for the Oldroyd 6-constant model [5]; King and Waters were the first to predict the transient velocity overshoot, and they used a linear viscoelastic model [6]; many authors have used the second-order fluid model to study closely related problems [7–9]. In

^{*} Corresponding author. Tel.: +1 919 636 1102.

E-mail addresses: nickmoore83@gmail.com, moore@cims.nyu.edu (M.N.J. Moore).

URL: <http://cims.nyu.edu/~moore/> (M.N.J. Moore).

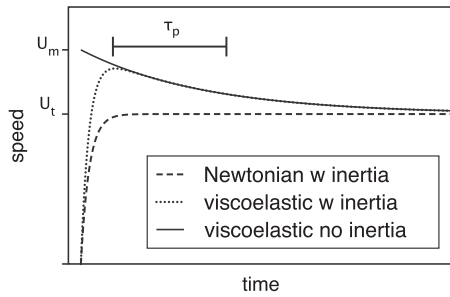


Fig. 1. Pictorial representation of the transient velocity overshoot.

a study that does not fit into either of the two categories above, Harlen used a boundary layer approximation, the so-called birefringent strand technique [10], to calculate the flow structure and drag coefficient in steady-state for finitely extensible (FENE) dumbbell models [11].

Recently more effort has been devoted to direct numerical simulation of non-linear viscoelastic models, including the simplest dumbbell models such as the Oldroyd-B (OB) and Upper Convected Maxwell (UCM) models [12,2,13], as well as the more elaborate FENE and Phan–Thien–Tanner models [14,3,4]. In most cases, simulations of the OB and UCM models are limited to a particular range of Wi (typically Wi less than 2 or so) due to apparent singular behavior of the stress field [12,2,13]. In the absence of analytical results, it is not clear whether this limitation is numerical or if it is of a more fundamental nature, such as a criticality of the constitutive equations.

As a step towards an analytical framework, we calculate solutions to the OB equations that are valid in the ‘weak-coupling’ limit of fixed Wi and $\beta \ll 1$. One way to approach this limit is to fix τ_p , V and L , while letting $\eta_s/\eta_p \rightarrow 0$. This is closely related to the diluteness criterion of a Boger fluid, $\eta_p/\eta_s \ll 1$, and is a physically relevant regime. Our semi-analytical results qualitatively match previous experimental observations, both in the transient and steady-state. For Wi larger than 2 or so, we present new findings for the OB model in the weak-coupling limit, including a modification of the overshoot time-scale and a scaling law for the steady-state drag as a function of Wi .

As a consequence of the weak-coupling expansion, an approximate polymeric stress evolves according to a leading-order Newtonian flow. The response of an immersed body is then determined using both the polymeric stress and the stress induced by a velocity-field correction. While the results are not entirely analytical, the computational component is reduced to evolving the Lagrangian variables forward in time with a prescribed velocity field and then solving a set of independent, linear ordinary differential equations (ODEs); all other calculations are simply evaluation of exact formulae. An attractive feature of the method is that the ODEs are independent of Wi . Other authors have also used a background Newtonian flow to evolve a polymeric stress field, but for the purpose of analyzing the stress structure formed near stagnation points or near boundaries [15–20]. In these instances the background Newtonian flow was assumed for convenience, whereas here it arises naturally from the expansion and additionally the resulting polymeric stress is used to correct body-dynamics.

For sufficiently large Wi , we observe the formation of a birefringent strand, as has been previously observed in a variety of situations and has been analyzed in great depth [21,10,11,22,16,18,19]. Through analysis of the birefringent strand, we show that for any Wi the polymeric stress stays bounded for all time and we determine its scaling with Wi . The time-boundedness of the polymeric stress is a consequence of the quadratic flow near the sphere’s rear stagnation point. This should be contrasted to a linear hyperbolic

flow where the polymeric stress has been found to grow unbounded in time [23]. We show our analysis of the birefringent strand to be consistent with a scaling law observed in the weak-coupling computations relating the drag and Wi . Additionally, we extend the weak-coupling method to the problem of a sphere settling with an oscillatory force and show how the introduction of a second time-scale influences the dynamic motion of the body.

2. Weak-coupling expansion

2.1. Formulation

Consider a heavy body descending in a viscoelastic fluid. We neglect both fluid and body inertia, i.e. $Re \ll 1$. The body’s motion is characterized by its translational velocity $\mathbf{U}(t)$ and its angular velocity $\mathbf{\Omega}(t)$. The evolution of these quantities is coupled to the fluid, and we take the incompressible Stokes Oldroyd-B equations (Stokes OB) as the governing fluid-model. In the Stokes OB model, the stress tensor is decomposed into the usual Newtonian stress tensor $\boldsymbol{\sigma}^N$ associated with the solvent, and an additional polymeric stress tensor $\boldsymbol{\sigma}^p$ arising from stretching, rotation, and relaxation of polymers in the solvent. The polymeric stress evolution is characterized by an elastic modulus G and a relaxation time-scale τ_p . The Newtonian stress tensor is given by $\boldsymbol{\sigma}^N = -p\mathbf{I} + \eta_s(\nabla\mathbf{u} + \nabla\mathbf{u}^T)$ where p is the pressure, η_s is the solvent viscosity, and \mathbf{u} is the divergence-free velocity field. The total stress tensor is $\boldsymbol{\sigma} = \boldsymbol{\sigma}^N + \boldsymbol{\sigma}^p$.

Consider a uniform-density sphere in an infinite fluid domain Ω , with the sphere surface denoted by $\partial\Omega$. In a Newtonian fluid of viscosity η_s , a sphere of radius L descends with speed $V = (2/9)g\Delta\rho L^2/\eta_s$, where g is the gravitational constant and $\Delta\rho$ is the density difference between the sphere and the fluid. We take V as a characteristic velocity for non-dimensionalization, although this is not necessarily the velocity of the sphere in the viscoelastic medium. Scaling space by L , time by L/V , and $\boldsymbol{\sigma}^p$ by G , gives the dimensionless form of the Stokes OB system,

$$-\nabla p + \Delta\mathbf{u} + \beta \nabla \cdot \boldsymbol{\sigma}^p = 0, \quad (1)$$

$$Wi \mathcal{D}_t[\mathbf{u}]\boldsymbol{\sigma}^p + (\boldsymbol{\sigma}^p - \mathbf{I}) = 0, \quad (2)$$

$$\int_{\partial\Omega} (\boldsymbol{\sigma}^N + \beta\boldsymbol{\sigma}^p) \cdot \hat{\mathbf{n}} \, dS = 6\pi\mathbf{e}_z, \quad (3)$$

$$\int_{\partial\Omega} \hat{\mathbf{x}} \times [(\boldsymbol{\sigma}^N + \beta\boldsymbol{\sigma}^p) \cdot \hat{\mathbf{n}}] \, dS = 0. \quad (4)$$

Here, the upper-convected time-derivative is $\mathcal{D}_t[\mathbf{u}]\boldsymbol{\sigma} \equiv \partial_t\boldsymbol{\sigma} + (\mathbf{u} \cdot \nabla)\boldsymbol{\sigma} - (\nabla\mathbf{u} \cdot \boldsymbol{\sigma} + \boldsymbol{\sigma} \cdot \nabla\mathbf{u}^T)$. The Weissenberg number, $Wi = \tau_p V/L$, is the ratio of the fluid relaxation time-scale to a flow time-scale, while $\beta = GL/(\eta_s V)$ measures the relative contribution of the polymeric stress to momentum balance. The product of the two is the ratio of polymeric viscosity to solvent viscosity, $\beta Wi = G\tau_p/\eta_s = \eta_p/\eta_s$, and the fluid has total dimensionless viscosity $1 + \beta Wi$ (sum of Newtonian and polymeric viscosities). The total stress tensor is $\boldsymbol{\sigma} = \boldsymbol{\sigma}^N + \beta\boldsymbol{\sigma}^p$ in this dimensionless form. Eq. (3) is the force balance on the body with a constant external gravitational force, and Eq. (4) is the torque balance on the body. Here, $\hat{\mathbf{n}}$ is the outward surface normal and $\hat{\mathbf{x}}$ is a vector originating at the sphere’s center of mass. The boundary conditions are no-slip on the surface of the body, and if we work in the body-frame, \mathbf{U} and $\mathbf{\Omega}$ are determined by the velocity field \mathbf{u} at infinity. Eqs. (1)–(4) form an initial value problem for $\mathbf{U}(t), \mathbf{\Omega}(t)$, and $\boldsymbol{\sigma}^p(\mathbf{x}, t)$. For a uniform density sphere and the initial condition $\boldsymbol{\sigma}^p(\mathbf{x}, 0) = \mathbf{I}$, the resulting symmetry of Eqs. (3) and (4) give $\mathbf{U}(t) = U(t)\mathbf{e}_z$ and $\mathbf{\Omega}(t) = 0$, i.e. vertical velocity and no rotation of the body. Again, we have assumed both the fluid and body inertia are negligible, implying that fluid and body velocities respond instantaneously to forces.

We consider Eqs. (1)–(4) for fixed Wi and $\beta \ll 1$. Since β measures the strength of coupling between the polymeric stress and

the momentum balance, we term this the weak-coupling limit. We formally expand all variables in a regular perturbation series in β ,

$$\mathbf{u}(\mathbf{x}, t) = \mathbf{u}_0(\mathbf{x}, t) + \beta \mathbf{u}_1(\mathbf{x}, t) + \mathcal{O}(\beta^2), \quad (5)$$

$$p(\mathbf{x}, t) = p_0(\mathbf{x}, t) + \beta p_1(\mathbf{x}, t) + \mathcal{O}(\beta^2), \quad (6)$$

$$\boldsymbol{\sigma}^p(\mathbf{x}, t) = \boldsymbol{\sigma}_0^p(\mathbf{x}, t) + \beta \boldsymbol{\sigma}_1^p(\mathbf{x}, t) + \mathcal{O}(\beta^2), \quad (7)$$

$$U(t) = U_0(t) + \beta Wi U_1(t) + \mathcal{O}(\beta^2). \quad (8)$$

The Newtonian stress tensor at order β^k is given by $\boldsymbol{\sigma}_k^N = -p_k \mathbf{I} + \nabla \mathbf{u}_k + \nabla \mathbf{u}_k^T$. $U(t)$ is the dimensionless sphere velocity in the vertical direction, and we have included the factor Wi in Eq. (8) for convenience. At order β^0 , Eqs. 1,3,4 reduce to

$$-\nabla p_0 + \Delta \mathbf{u}_0 = 0, \quad (9)$$

$$\int_{\partial\Omega} \boldsymbol{\sigma}_0^N \cdot \hat{\mathbf{n}} \, dS = 6\pi \mathbf{e}_z, \quad (10)$$

$$\int_{\partial\Omega} \hat{\mathbf{x}} \times \boldsymbol{\sigma}_0^N \cdot \hat{\mathbf{n}} \, dS = 0. \quad (11)$$

The solution is the well-known Stokes flow around a sphere under constant body force and zero torque, giving $U_0(t) = -1$. The exact formula for \mathbf{u}_0 is given in Appendix A.

At order β^0 , Eq. (2) linearly couples \mathbf{u}_0 and $\boldsymbol{\sigma}_0^p$,

$$Wi \mathcal{D}_t[\mathbf{u}_0] \boldsymbol{\sigma}_0^p + (\boldsymbol{\sigma}_0^p - \mathbf{I}) = 0. \quad (12)$$

At order β^1 , Eq. (1) gives the linear inhomogeneous Stokes equation,

$$-\nabla p_1 + \Delta \mathbf{u}_1 = -\nabla \cdot \boldsymbol{\sigma}_0^p. \quad (13)$$

Also at order β^1 , Eq. (3) gives the integral constraint,

$$\int_{\partial\Omega} (\boldsymbol{\sigma}_1^N + \boldsymbol{\sigma}_0^p) \cdot \hat{\mathbf{n}} \, dS = 0, \quad (14)$$

while Eq. (4) is trivially satisfied by symmetry.

Given \mathbf{u}_0 , we discuss how to efficiently solve Eqs. (12)–(14) for $U_1(t)$, the first correction to the body-velocity. To orient the reader, we give a brief description of the expected behavior of U_1 . Since $U_0 = -1$, i.e. downward motion, positive U_1 implies a decrease of the sphere's descent rate. $U_1 = 1$ implies the sphere descends at the same rate that it would in a Newtonian fluid with viscosity $1 + \beta Wi$. Thus, $U_1 > 1$ corresponds to an enhanced drag compared to this Newtonian case, and $U_1 < 1$ corresponds to a drag reduction. As for the transient behavior, U_1 taking the form $1 - e^{-t/Wi}$ corresponds to a velocity overshoot with time-scale Wi and exponential saturation to steady-state. This behavior might be naively anticipated from linear-shear-flow rheology, and it qualitatively matches experiments on descending spheres [2,4]. We therefore refer to it as the 'anticipated' behavior of U_1 .

2.2. Method of solution

In this section, we introduce an efficient and simple solution technique for Eq. (12). Since $\{\mathbf{u}_0, p_0\}$ are known analytically, the direct solution of Eqs. (13) and (14) can be avoided, and U_1 can be obtained by use of the reciprocal theorem. We work in a spherical coordinate system $\mathbf{x} = (r, \theta, \varphi)$, where r is the radius, θ is the polar angle from the upwards pointing vertical direction \mathbf{e}_z , and φ is the azimuthal angle. Taking $\boldsymbol{\sigma}_0^p(\mathbf{x}, 0) = \mathbf{I}$ implies that $\boldsymbol{\sigma}_0^p(\mathbf{x}, t)$ is independent of φ , and thus the flow remains axisymmetric for all time.

In the Lagrangian frame, Eq. (12) can be written as

$$Wi \frac{D}{Dt} (\mathbf{F}^{-1} \boldsymbol{\sigma}_0^p \mathbf{F}^{-T}) + \mathbf{F}^{-1} \boldsymbol{\sigma}_0^p \mathbf{F}^{-T} = \mathbf{F}^{-1} \mathbf{F}^{-T}. \quad (15)$$

Here $\mathbf{F} = \partial \mathbf{X} / \partial \boldsymbol{\alpha}$, where $\mathbf{X}(\boldsymbol{\alpha}, t)$ is the Lagrangian flow map taking a fluid tracer from initial position $\boldsymbol{\alpha}$ to position \mathbf{X} at time t . D/Dt is the time-derivative in the Lagrangian frame. \mathbf{F} is known as the

deformation gradient, or the Jacobian of the flow map \mathbf{X} , and it evolves according to

$$\frac{D}{Dt} \mathbf{F}(\boldsymbol{\alpha}, t) = \nabla \mathbf{u}_0(\mathbf{X}(\boldsymbol{\alpha}, t)) \mathbf{F}(\boldsymbol{\alpha}, t). \quad (16)$$

Using an integrating factor, the solution to Eq. (15) is

$$\begin{aligned} \boldsymbol{\sigma}_0^p(\boldsymbol{\alpha}, t) &= e^{-t/Wi} \mathbf{F}(\boldsymbol{\alpha}, t) \boldsymbol{\sigma}_0^p(\boldsymbol{\alpha}, 0) \mathbf{F}^T(\boldsymbol{\alpha}, t) + \frac{1}{Wi} \\ &\times \int_0^t ds e^{-s/Wi} \mathbf{F}(\boldsymbol{\alpha}, t) \mathbf{F}^{-1}(\boldsymbol{\alpha}, t-s) \mathbf{F}^{-T}(\boldsymbol{\alpha}, t-s) \mathbf{F}^T(\boldsymbol{\alpha}, t). \end{aligned} \quad (17)$$

To evaluate this exact formula, we first evolve $\mathbf{X}(\boldsymbol{\alpha}, t)$ forward in time with a fourth-order Runge–Kutta method. Since Eq. (16) is linear, $\mathbf{F}(\boldsymbol{\alpha}, t)$ can be evolved with a semi-implicit method, and we use a fourth-order Adams–Moulton method for this. We then evaluate Eq. (17) with a fourth-order Simpson's quadrature, yielding a solution for $\boldsymbol{\sigma}_0^p(\boldsymbol{\alpha}, t)$ that is fourth-order accurate in Δt . We emphasize that the point-wise accuracy of the solution does not depend on a spatial discretization parameter.

Let \mathbf{u}^A and \mathbf{u}^B be two incompressible velocity fields with associated stress tensors $\boldsymbol{\sigma}^A$ and $\boldsymbol{\sigma}^B$. Assuming both velocity fields decay sufficiently fast at infinity and that $\nabla \cdot \boldsymbol{\sigma}^A = 0$, the reciprocal theorem gives

$$\int_{\Omega} \mathbf{u}^A \cdot (\nabla \cdot \boldsymbol{\sigma}^B) \, dV - \int_{\partial\Omega} \mathbf{u}^A \cdot \boldsymbol{\sigma}^B \cdot \hat{\mathbf{n}} \, dS = - \int_{\partial\Omega} \mathbf{u}^B \cdot \boldsymbol{\sigma}^A \cdot \hat{\mathbf{n}} \, dS, \quad (18)$$

Taking $\mathbf{u}^A = \mathbf{u}_0 - 1\mathbf{e}_z$, $\mathbf{u}^B = \mathbf{u}_1 + Wi U_1 \mathbf{e}_z$, and using Eqs. (13) and (14), and an integration by parts, gives

$$U_1(t) = \frac{1}{6\pi Wi} \int_{\Omega} \nabla \mathbf{u}_0(\mathbf{x}, t) : \boldsymbol{\sigma}_0^p(\mathbf{x}, t) \, dV. \quad (19)$$

We compute this integral numerically by forming a Delaunay triangulation of the Lagrangian grid, then integrating with a second-order accurate method based on linear-interpolation within each triangle. We truncate the integration region at an outer radius R_{max} and use Richardson extrapolation in R_{max} to approximate the infinite-domain integral in Eq. (19). This completes what we call the weak-coupling numerical method. Here, we have avoided directly solving Eqs. (13) and (14) for $\{\mathbf{u}_1, p_1\}$, however in principle this could be done in a relatively straightforward fashion. The solution to the forced Stokes equation, Eq. (13), may be represented by a distribution of Stokeslets, and Eq. (14) may be satisfied by adding a multiple of the homogeneous solution $\{\mathbf{u}_0, p_0\}$.

To better understand the integrand in Eq. (19), let

$$\Phi(\mathbf{x}, t) \equiv \frac{4}{9Wi} \nabla \mathbf{u}_0 : \boldsymbol{\sigma}_0^p. \quad (20)$$

Here the multiplicative factor is chosen for convenience. The relative strain energy (to leading order in β) is given by $\mathcal{E}(t) = (1/2) \int_{\Omega} \text{tr}(\boldsymbol{\sigma}_0^p(\mathbf{x}, t) - \mathbf{I}) \, dV$, and so we can define a strain energy density as $\gamma(\mathbf{x}, t) = (1/2) \text{tr}(\boldsymbol{\sigma}_0^p(\mathbf{x}, t) - \mathbf{I})$. Taking a time derivative in the Lagrangian frame gives $D\gamma/Dt + Wi^{-1}\gamma = (9/4)Wi \Phi$. Therefore, Φ controls the rate at which elastic energy is stored locally.

We supplement the numerical evaluation of Eqs. (17) and (19) with a few analytical results. First, on the sphere surface, Eq. (17) can be evaluated exactly and this is given in Appendix A. This exact solution is useful for benchmarking the numerics. Next, in the fluid bulk we have found a formal series solution to Eqs. (17) and (19) in the variables Wi and t/Wi , and this is given in Appendix B. Surprisingly, the series is a single summation that is ordered in both Wi and t/Wi . When truncated it provides either low- Wi or short-time asymptotic information.

3. Results

3.1. Steady-state, low- Wi benchmark

In steady-state and at low Weissenberg number, a sphere descends at nearly the same rate as in a Newtonian fluid with viscosity $1 + \beta Wi$, but with a slight velocity increase, or drag reduction. This behavior has been predicted previously [5] and has been observed experimentally, though with a much more substantial drag reduction due to the presence of device walls (see [1,3] for example). The low- Wi asymptotic solution of Leslie and Tanner [5] can be used to benchmark our numerical computations. Additionally, our series solution given in Appendix B recovers the result of Leslie and Tanner when truncated at order Wi^2 , while the successive terms allow for a more detailed benchmark of the computations.

Let $U_1^\infty = \lim_{t \rightarrow \infty} U_1(t)$ be the steady-state velocity correction. Fig. 2 shows $1 - U_1^\infty$ computed by the weak-coupling method, along with the series solution in Eq. (B.11) truncated at orders Wi^2 and Wi^{12} . The figure shows agreement between all three as $Wi \rightarrow 0$, with an error less than 10^{-4} (the dominant source of numerical error is the spatial integration of Eq. (19)). Recall that $U_1 < 1$ corresponds to a drag reduction, and notice that the drag reduction is very slight with a magnitude always less than 3×10^{-3} .

3.2. Steady-state results for varying Wi

For Wi not small we rely exclusively on the weak-coupling numerical method to determine U_1 , and we first consider the

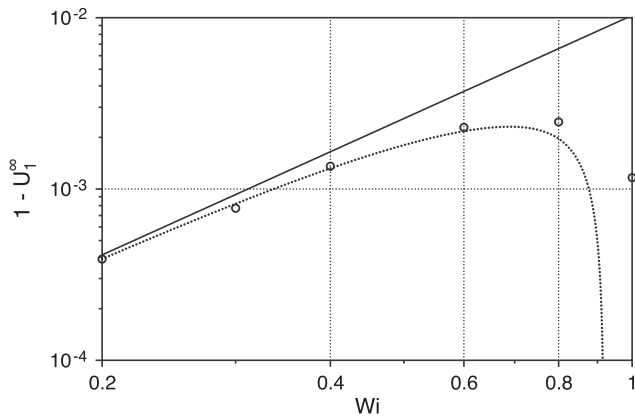
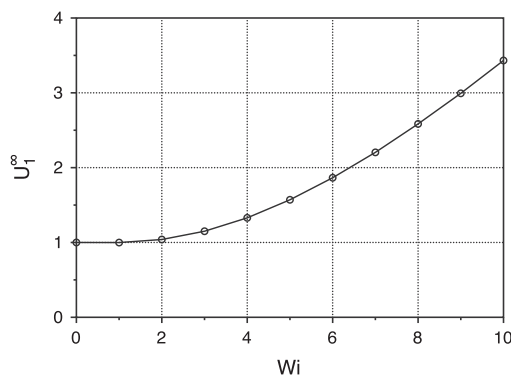
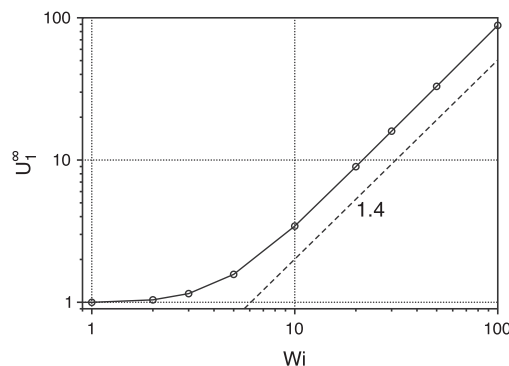


Fig. 2. $1 - U_1^\infty$ computed by the weak-coupling method (circles) and the asymptotic formula (B.11), retaining terms up to Wi^2 (solid line) and Wi^{12} (dotted curve).



(a) Lin-lin axes



(b) Log-log axes

Fig. 3. The steady-state velocity correction, U_1^∞ , as Wi is varied.

steady-state behavior. Fig. 3a shows U_1^∞ increasing with Wi after a notably flat departure from $U_1^\infty = 1$ at $Wi = 0$. Recall that an increase in U_1^∞ implies a slow-down of the sphere, or equivalently an enhanced drag. Fig. 3b shows the same plot on a log-log scale, indicating a power-law scaling of roughly $U_1^\infty \sim Wi^{1.4}$ for large Wi . The prediction of enhanced drag for increasing Wi is in qualitative agreement with experiments [1–3], while the scaling law is a new finding for the Stokes OB model, at least within the weak coupling approximation.

Recall that U_1 is determined by the integration of Φ in Eq. (19), and that Φ represents the local storage rate of elastic energy. Steady-state distributions of Φ , as shown in Fig. 4, offer insight into the behavior of U_1^∞ . For low Wi , Φ is concentrated near the waist of the sphere and is nearly fore-aft symmetric (see Fig. 4a). In fact, Appendix B shows that in steady-state, $\Phi = (4/9) \nabla \mathbf{u}_0 : (\nabla \mathbf{u}_0 + \nabla \mathbf{u}_0^T) + \mathcal{O}(Wi)$, a formula which accounts for the fore-aft symmetry. Integrating this formula gives $U_1^\infty \sim 1$ for $Wi \ll 1$, in agreement with Fig. 3. For $Wi = 2$, a region of large Φ appears above the rear stagnation point, where the bulk fluid is most effectively stretched (Fig. 4b). Large Wi corresponds to long fluid-memory, meaning that a Lagrangian tracer in the wake can be strongly influenced by its history near the rear stagnation point. This is seen dramatically in Fig. 4c for $Wi = 5$, as Φ becomes increasingly concentrated in the wake and a birefringent strand emerges. The presence of the birefringent strand accounts for the increase in U_1^∞ seen in Fig. 3.

3.3. Dynamic results

To illustrate the dynamic behavior predicted by the weak-coupling method, Fig. 5a shows $U_1(t/Wi)$ normalized by its steady-state value U_1^∞ . For low Wi , U_1 follows the anticipated behavior $1 - e^{-t/Wi}$ closely. Recall this corresponds to a velocity overshoot with time-scale Wi and magnitude βWi – behavior that is in qualitative agreement with experimental observations. Increasing Wi modifies this behavior, and the transient time-scale becomes larger than Wi (see Fig. 5a). The most dramatic changes occur for $Wi = 3-10$. For $Wi \geq 10$, a change in the concavity of U_1/U_1^∞ is visible, from concave up at short times to concave down at longer times. Increasing Wi beyond 20 modifies U_1^∞ (as shown in Fig. 3b), but little change is visible in the dynamic quantity U_1/U_1^∞ .

Much like before, the distribution of Φ is helpful to understand the behavior of U_1 . Fig. 6 shows the development of Φ for $Wi = 2$. In this case, Φ grows to roughly the same magnitude in the region around the waist of the sphere (region 1) as it does in the region aft of the rear stagnation point (region 2), allowing for a comparison of the dynamics in the two regions. We have observed the development of Φ in region 1 to be well described by the low- Wi

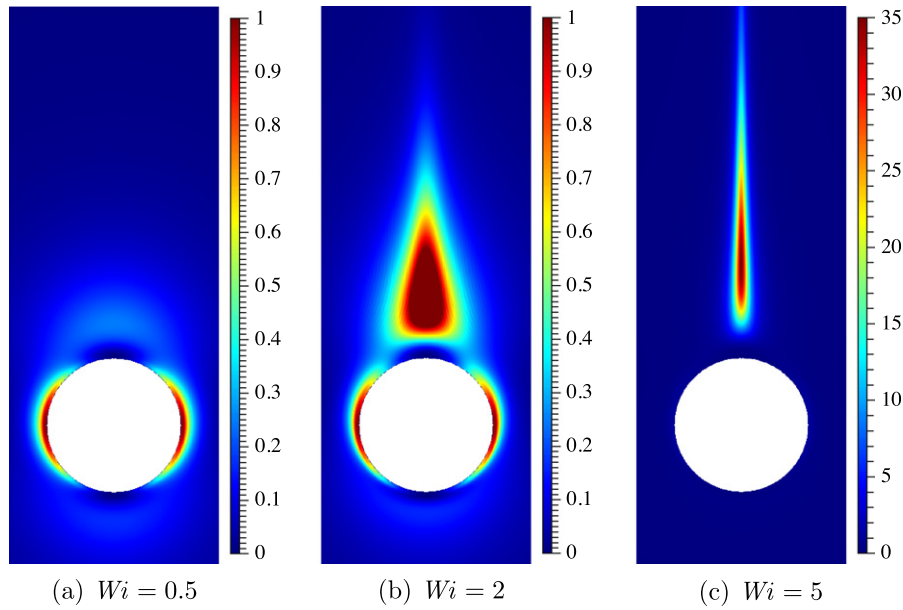


Fig. 4. The steady-state distribution of Φ for increasing Wi . The flow is from bottom to top. Note the appearance of a birefringent strand in (c) and the difference in the scale-bar.

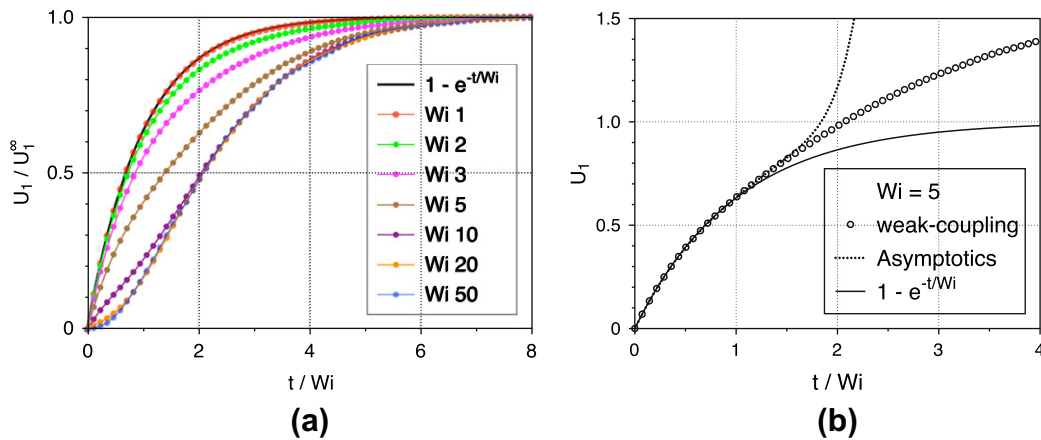


Fig. 5. (a) $U_1(t/Wi)$ normalized by U_1^∞ for several values of Wi . (b) $U_1(t/Wi)$ from the weak-coupling method with $Wi = 5$ (circles), along with the series solution (B.11) truncated at order $(t/Wi)^{12}$ (dotted curve), and the simple exponential saturation (solid curve).

approximation given in Appendix B, $\Phi \sim (4/9) \nabla \mathbf{u}_0 : (\nabla \mathbf{u}_0 + \nabla \mathbf{u}_0^T)(1 - e^{-t/Wi})$, even for Wi not small. This observation is consistent with the exact solution on the sphere surface, $\Phi = \sin^2\theta(1 - e^{-t/Wi})$, which depends only on t/Wi and not Wi (see Appendix A). Integrating the low- Wi formula gives $U_1 \sim 1 - e^{-t/Wi}$. This, together with the observation that the low- Wi formula always appears to be valid in region 1, suggests that the development of Φ in region 1 accounts for purely exponential saturation of U_1 . This purely exponential saturation prevails for low- Wi because Φ is primarily concentrated in region 1.

Now consider region 2. Here, Φ develops over a longer time-scale, roughly $t/Wi = 8$ for the case shown in Fig. 6. The contribution of Φ in this region modifies the purely exponential saturation of U_1 and accounts for the longer transient observed for $Wi > 1$ (see Fig. 5a). For $Wi = 5$, Fig. 7 shows the emergence of the birefringent strand, which causes further modification to the U_1 -transient. Here, Φ is dominantly concentrated in region 2. The development

of Φ in region 1 is again described by the low- Wi formula, but is not visible in the figure due to the change in scale.

The series solution given in Appendix B also lends insight into the transient behavior of U_1 , in particular the departure from exponential-in-time saturation. Recall that the truncation of series (B.11) provides both low- Wi and short-time information. Fig. 5b shows U_1 for $Wi = 5$ fixed, plotted against the series (B.11) truncated at order $(t/Wi)^{12}$. As seen in the figure, the truncated series captures the initial departure from exponential saturation, however loses accuracy at larger time. It is interesting to consider how the transient time-scale becomes modified in this series solution. Inspection reveals that terms of the form $(t/Wi)^k e^{-t/Wi}$ enter at order Wi^n , where $k < n$. The function $(t/Wi)^k e^{-t/Wi}$ is maximized at $t/Wi = k$, and so this gives rise to an integer multiple of the basic time-scale Wi . A more complete analysis of the transient modification could also incorporate the decay rate of the coefficients, and this is left for future study.

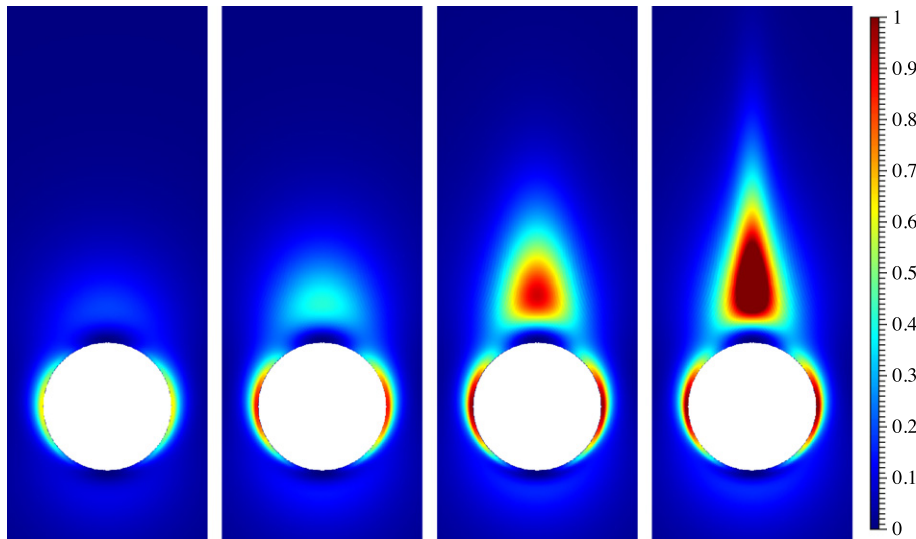


Fig. 6. Time sequence of Φ with $Wi = 2$ and $t/Wi = 1, 2, 4, 8$, moving from left to right.

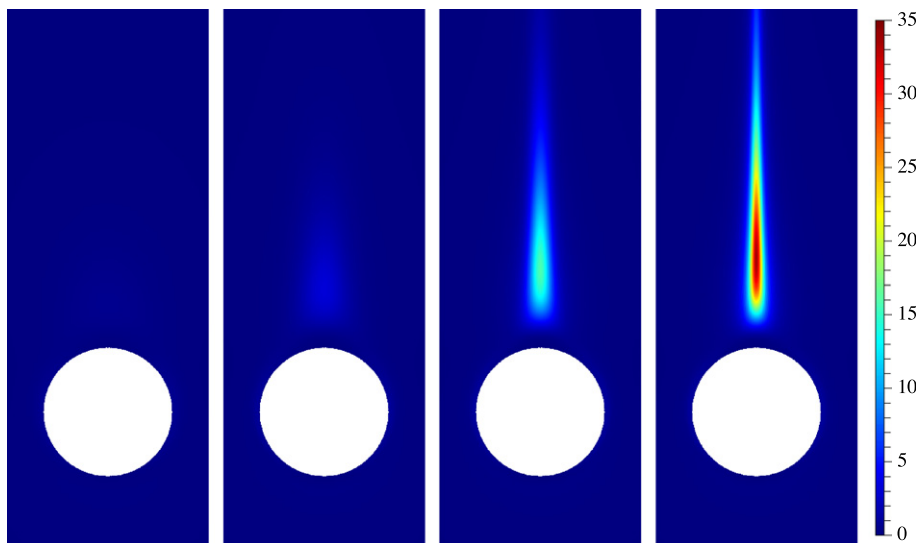


Fig. 7. Time sequence of Φ with $Wi = 5$ and $t/Wi = 1, 2, 4, 8$, moving from left to right.

4. Birefringent strand analysis

4.1. Boundedness of the polymeric stress

The validity of the weak-coupling expansion relies on the assumption that σ_0^p remains bounded in time so that the higher order terms in the expansion remain small. It is therefore important to investigate the possibility of the polymeric stress becoming singular, particularly in light of previous suggestions to this possibility [24,13]. In this section we demonstrate the time-boundedness of σ_0^p everywhere in the fluid domain. The rear stagnation line, located on the central-axis of the birefringent strand, requires special care in the argument. It is not evident whether higher-order spatial derivatives of σ_0^p remain bounded or not, and this is an important topic to be considered in the future.

We first demonstrate the boundedness of σ_0^p in the portion of the fluid domain excluding the sphere surface and the rear stagnation line, here called Ω_1 . The main idea is that characteristics can be evolved backwards in time to solve for the deformation gradient and demonstrate its boundedness, and σ_0^p inherits this feature

through the exact relation given in Eq. (17). To this end, consider a fixed Eulerian point $\mathbf{x}_1 \in \Omega_1$, and let $\mathbf{H}(t)$ satisfy $d\mathbf{H}/dt = -\nabla\mathbf{u}_0(\mathbf{X}(\mathbf{x}_1, -t))$ with $\mathbf{H}(0) = \mathbf{I}$. Let $\mathbf{G}(\mathbf{X}(\alpha, t), t) \equiv \mathbf{F}(\alpha, t)$, with initial condition $\mathbf{G}(\mathbf{x}, 0) = \mathbf{I}$, i.e. \mathbf{G} is the deformation gradient in the Eulerian frame. Then $\mathbf{G}(\mathbf{x}_1, t) = \mathbf{H}(t)^{-1}$ for all time (we have simply reversed the time-evolution). $\mathbf{x}_1 \in \Omega_1$ implies that $\mathbf{X}(\mathbf{x}_1, -t) = (r, \theta, \phi) \rightarrow (\infty, \pi, \phi)$ as $t \rightarrow \infty$, where $\nabla\mathbf{u}_0$ becomes diagonal and decays like r^{-2} . The flow becomes uniform far away from the body, implying $r(t) = \mathcal{O}(t)$ as $t \rightarrow \infty$, and therefore $\nabla\mathbf{u}_0(\mathbf{X}(\mathbf{x}_1, -t)) \sim \mathcal{O}(t^{-2})$. This decay rate is sufficiently fast that $\mathbf{H}(t)$ approaches a constant value, i.e. $\mathbf{H}^\infty \equiv \lim_{t \rightarrow \infty} \mathbf{H}(t)$ exists and is finite. Recalling $\det \mathbf{G} = 1$, implies that $\det \mathbf{H}(t) = 1$ for all time and thus \mathbf{H}^∞ is invertible. Upon inversion, this shows that $\mathbf{G}(\mathbf{x}_1, t)$ remains bounded for all time. With the deformation gradient bounded in time, Eq. (17) shows that σ_0^p remains bounded in time for any Wi , and further that $\lim_{t \rightarrow \infty} \sigma_0^p = \mathcal{O}(Wi)$ for $Wi \gg 1$. For points on the sphere surface, the exact solutions in Appendix A show that \mathbf{F} grows linearly in time whereas σ_0^p remains bounded for all time. Here, $\lim_{t \rightarrow \infty} \sigma_0^p = \mathcal{O}(Wi^2)$ for $Wi \gg 1$.

This leaves the rear stagnation line, defined by $\theta = 0$. Here, $\nabla\mathbf{u}_0$ is diagonal implying that Eq. (16) decouples and \mathbf{F} remains

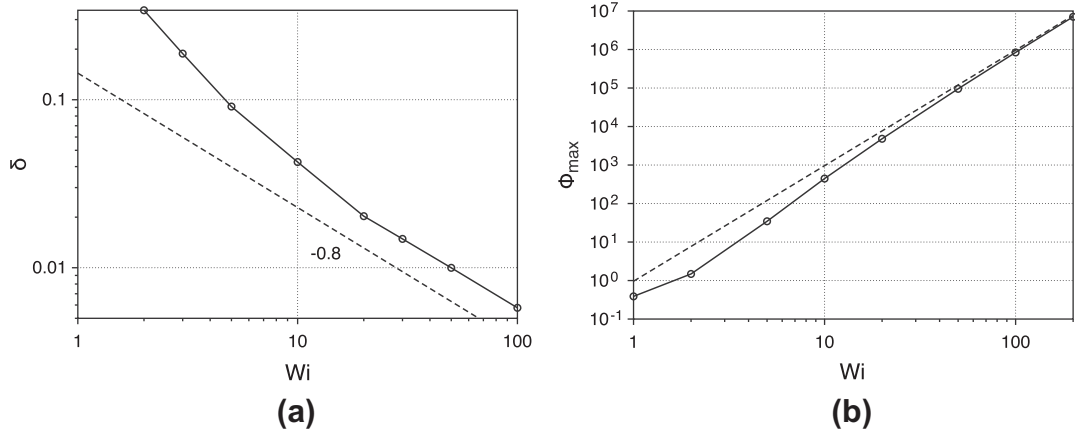


Fig. 8. (a) Estimate of δ for varying Wi from the weak-coupling method (solid line with circles) along with a power law $Wi^{-0.8}$ (dashed line). (b) Φ_{max} as a function of Wi from the weak-coupling method (solid line with circles) and the asymptotic prediction $0.96Wi^3$ from Eq. (23) (dashed line).

diagonal. Let $\mathbf{X} = (r, 0, 0)$ and $\boldsymbol{\alpha} = (r_0, 0, 0)$. By changing the independent variable from t to r in the evolution equation, it is possible to solve for \mathbf{F} exactly. The first component is

$$F_{11}(r, r_0) = \left(\frac{r}{r_0}\right)^3 \left(\frac{1+2r}{1+2r_0}\right) \left(\frac{1-r}{1-r_0}\right)^2, \quad (21)$$

The other components are determined by $F_{22} = F_{33} = F_{11}^{-1/2}$, which follows from axisymmetry and that $\det \mathbf{F} = F_{11} \cdot F_{22} \cdot F_{33} = 1$. For a fixed r , we have $r_0 \rightarrow 1$ as $t \rightarrow \infty$, i.e. back towards the stagnation point, which through Eq. (21) implies that F_{11} grows unbounded in time. Near the stagnation point the flow is locally quadratic, $u_r \sim 3/2 (r-1)^2$, giving $r_0 \sim 1 + 2/3 t^{-1}$ as $t \rightarrow \infty$. When inserted into Eq. (21) this implies that $F_{11} \sim C(r) t^2$, where $C(r) = 3/4 r^{-3} (1+2r)(1-r)^2$, that is the deformation gradient grows quadratically over long time. This should be contrasted with the behavior near a linear hyperbolic point, where the deformation gradient grows exponentially in time and leads to exponential growth of the polymeric stress past a critical Weissenberg number [23]. Here however, the quadratic growth rate of \mathbf{F} implies through Eq. (17) that $\boldsymbol{\sigma}_p^0$ remains bounded for all time and gives

$$\lim_{t \rightarrow \infty} \sigma_{11}|_{\theta=0} \sim \frac{27}{2} \frac{(1+2r)^2 (r-1)^4}{r^6} Wi^4 \quad \text{for } Wi \gg 1, \quad (22)$$

where σ_{11} denotes the (1,1) entry of $\boldsymbol{\sigma}_p^0$. This expression has been checked directly with our numerical computation. It can be compared to a similar result for flow around a cylinder, in which the polymeric stress has been determined to grow as Wi^3 along the rear stagnation line and as Wi^5 in a narrow region surrounding the rear stagnation line [15,16].

The preceding argument proves that within the weak-coupling limit of the Stokes OB model, the polymeric stress remains bounded for all time everywhere in the fluid domain. The most essential points of the argument are that the flow is locally quadratic near the rear stagnation point and that the flow tends to a uniform velocity far away from the body. An interesting question not addressed here is whether these points can be applied to the fully-coupled Stokes OB model (i.e. with β not assumed small) in order to prove the boundedness of the polymeric stress more generally for the descending sphere problem. Previous results regarding hyperbolic stagnation flows suggest that the growth of the polymeric stress may even be ameliorated by retaining the coupling [23].

4.2. U_1^∞ for large Wi

Here we present some brief analysis of the birefringent strand that shows consistency with the scaling law $U_1^\infty \sim Wi^{1.4}$ observed in Section 3.2. We use Eq. (22) along with the exact formula for $\nabla \mathbf{u}_0$, given in Appendix A, to determine Φ asymptotically along the rear stagnation line,

$$\Phi_{BS}(r) \equiv \lim_{t \rightarrow \infty} \Phi|_{\theta=0} \sim \frac{9(r+1)(r-1)^5(1+2r)^2}{r^{10}} Wi^3 \quad \text{for } Wi \gg 1. \quad (23)$$

The BS stands for ‘birefringent strand’. Assume that this scaling holds approximately within some narrow region defined by $-\delta < r \sin \theta < \delta$ and $1 < r < E$, so that the region’s width is 2δ and its extent is E , both of which may depend on Wi . Φ is integrated in Eq. (19) to determine U_1^∞ , and the distribution of Φ is dominated by that in the birefringent strand for large Wi . Therefore we can consider Φ only in this narrow region to determine how U_1^∞ scales with large Wi .

Observations from the weak-coupling method show $E \rightarrow \infty$ and $\delta \rightarrow 0$ as $Wi \rightarrow \infty$. Eq. (23) is integrable in r , and so to leading order in large Wi , $U_1^\infty \sim \delta^2 \int_0^\infty \Phi_{BS}(r) dr$; the dependence on E will enter at higher order. From the weak-coupling method, we measure the half-width-at-half-maximum of Φ along the birefringent strand in order to estimate δ . We observe the scaling $\delta \sim Wi^{-0.8}$, as shown in Fig. 8, with an error estimate of roughly 0.05 in the exponent. Fig. 8 shows the maximum of $\Phi_{BS}(r)$, denoted Φ_{max} , computed from the weak-coupling method, which agrees with Eq. (23) as $Wi \rightarrow \infty$. Inserting the numerically determined scaling of δ and the analytically determined scaling of $\Phi_{BS}(r)$ gives $U_1^\infty \sim Wi^{1.4}$, as was already observed in Section 3.2. An entirely analytical derivation of the scaling law seems possible and we leave that for future study. We remind the reader that the weak-coupling limit applies to fixed Wi and $\beta \ll 1$, and so the smallness criterion for β may depend on Wi , in particular as Wi grows large.

5. Oscillatory body-force

In this section, we consider an extension of the settling body problem by adding an oscillatory body-force. This introduces another time-scale that can potentially be played off of the two time-scales already present, L/V and τ_p . Recent theoretical and experimental studies have suggested that the speed of a swimming organism can be substantially modified in a viscoelastic fluid [25–28], especially when its beat-frequency is in resonance with the fluid relaxation time [26,28]. The oscillatory force problem can

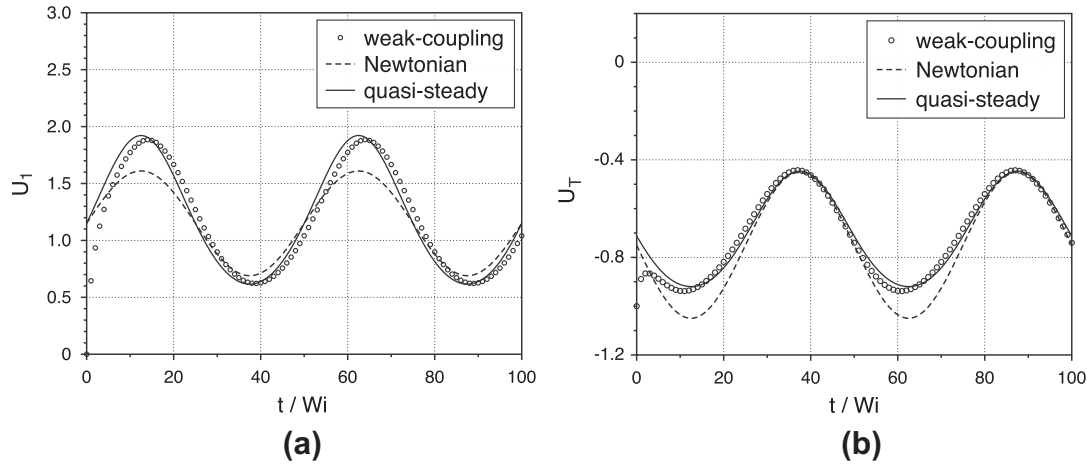


Fig. 9. (a) U_1 from an oscillatory flow with $A = 0.4$ computed by the weak-coupling method (open circles) with $Wi = 3$ and $De = 0.02$, along with the Newtonian response, $f(t)U_1^\infty(Wi)$ (dashed curve), and the quasi-steady prediction $U_1^{QS}(t)$ defined in the text (solid curve). (b) U_T with $\beta Wi = 0.25$, along with the prediction for a Newtonian fluid (dashed curve) and the quasi-steady prediction (solid curve).

be considered a toy-model for self-propulsion that removes the complexities of shape change.

Consider an external body-force that oscillates with period τ_f . Let the Deborah number be defined as the ratio of the polymeric relaxation time to the forcing period, $De = \tau_p/\tau_f$. The mean of the oscillatory force is still the gravitational force on the body, and the relative amplitude of the oscillation is A . When the oscillatory force is inserted into the dimensionless Stokes OB equations, the only modification is to Eq. (3), which now becomes

$$\int_{\partial\Omega} (\boldsymbol{\sigma}^N + \beta\boldsymbol{\sigma}^p) \cdot \hat{\mathbf{n}} \, dS = 6\pi\mathbf{e}_z f(t), \quad (24)$$

where $f(t) \equiv 1 + A \sin(2\pi De t/Wi)$. We once again consider the weak-coupling limit of fixed Wi and $\beta \ll 1$, and apply the same methodology as before. The leading order sphere velocity is now given by $U_0 = -f(t)$. We use the weak-coupling Lagrangian method with background flow \mathbf{u}_0 (now time-dependent) to determine the stress field $\boldsymbol{\sigma}_0^p$, and then use the reciprocal theorem to determine U_1 .

A few special limits are useful to gain some initial insight. For Wi and De both small, one expects the fluid to behave essentially as a Newtonian fluid with viscosity $1 + \beta Wi$. It is therefore expected that $U_1 \sim f(t)$ for $Wi, De \ll 1$, and we have confirmed this directly with the weak-coupling numerical solution. The next limit to consider is Wi fixed and $De \ll 1$, corresponding to a slow oscillation. In this limit, the flow can be considered quasi-steady, allowing transients in the elastic response to be neglected. We can use the steady-state information provided by Fig. 3, and imagine traversing this plot by defining an effective Weissenberg number, $Wi_{\text{eff}}(t) \equiv f(t)Wi$. Then the quasi-steady response is $U_1^{QS} \equiv f(t)U_1^\infty(Wi_{\text{eff}}(t))$, where $U_1^\infty(Wi)$ is taken from a steady flow (i.e. the function depicted in Fig. 3).

Fig. 9a shows U_1 with $Wi = 3$ and $De = 0.02$, and shows good agreement between the weak-coupling method and the quasi-steady prediction. For comparison, the figure also shows the ‘Newtonian’ response $f(t)U_1^\infty(Wi)$, which would occur if the extra stress where simply Newtonian. Notice that the valleys of U_1 roughly align with the Newtonian response, but the peaks are substantially amplified. This can be attributed to the positive curvature of $U_1^\infty(Wi)$ in Fig. 3. Also note the slight phase difference between the numerical solution and both the Newtonian and quasi-steady predictions. This is to be expected, as it corresponds to a slight lag of the elastic response to the slowly changing flow. In Fig. 9b, we show how the elastic response affects the actual motion of the sphere by taking a non-vanishing β (we take $\beta Wi = 0.25$) and

then computing the total velocity (to first order in β), $U_T \equiv U_0 + \beta U_1$. Since U_1 is nearly in phase with the $f(t)$ it generally opposes U_0 , and the amplified peaks in U_1 act to reduce the amplitude of the valleys in U_T .

The opposite limit is an extremely fast oscillation, corresponding to a large Deborah number. Here the elastic stress does not have sufficient time to respond to the rapidly oscillating flow, and as a consequence the oscillations in U_1 are strongly damped. Fig. 10a shows U_1 compared to the Newtonian response for $Wi = 3$ and $De = 5$, and illustrates this damping. The effect this has on the total sphere velocity is quite the opposite, since U_1 generally opposes U_0 . Fig. 10b shows U_T and demonstrates that the oscillations are exaggerated as compared to a Newtonian fluid. This behavior can be captured through a simple high-Deborah-number model, by assuming that the elastic response is constant in time with the constant determined by the steady flow response $U_1^\infty(Wi)$. This gives for the total velocity $U_T^{HD} = -f(t) + \beta Wi U_1^\infty(Wi)$ (the superscript ‘HD’ stands for high Deborah). Therefore, the sphere descends with an average velocity that it would have in a Newtonian fluid with viscosity $1 + \beta Wi U_1^\infty(Wi)$, but with oscillations that it would have in a Newtonian fluid with viscosity 1. The high-Deborah-number model is shown in Fig. 10b and it compares favorably with the weak-coupling numerical solution.

The presence of viscoelasticity breaks the time-reversibility of Stokes flow, and so an interesting question is how the introduction of the oscillatory forcing changes the average velocity of the sphere when it is in a viscoelastic fluid. To study this, we compute the time-average of U_1 over a period, denoted $\langle U_1 \rangle$. Fig. 11a shows $\langle U_1 \rangle$ for several fixed values of Wi as De is varied continuously. For $Wi \leq 3$, $\langle U_1 \rangle$ depends weakly on De , with variations always less than 5%. For $Wi = 4$ and 5, the variations become somewhat stronger and reach roughly 10%. Note that in all cases, the largest variations occur for small De and that $\langle U_1 \rangle$ is essentially constant for $De > 0.5$. The average total velocity is given by $\langle U_T \rangle = \langle U_0 \rangle + \beta Wi \langle U_1 \rangle = -1 + \beta Wi \langle U_1 \rangle$. Thus the relative variations in $\langle U_T \rangle$ are smaller than those in $\langle U_1 \rangle$ by a factor of approximately βWi . For $\beta Wi = 0.25$, the variations in $\langle U_T \rangle$ are on the order of 1% for $Wi \leq 3$, and up to 2.5% for $Wi \leq 5$.

More notable are the differences in the amplitude of the oscillations, and this is depicted in Fig. 11b and c. As Fig. 11b shows, the amplitude of oscillation in U_1 decreases with increasing De and eventually behaves as De^{-1} for all of the Weissenberg numbers tested. The behavior of U_T is more complicated since it involves the amplitude of oscillation of U_1 as well as the phase difference

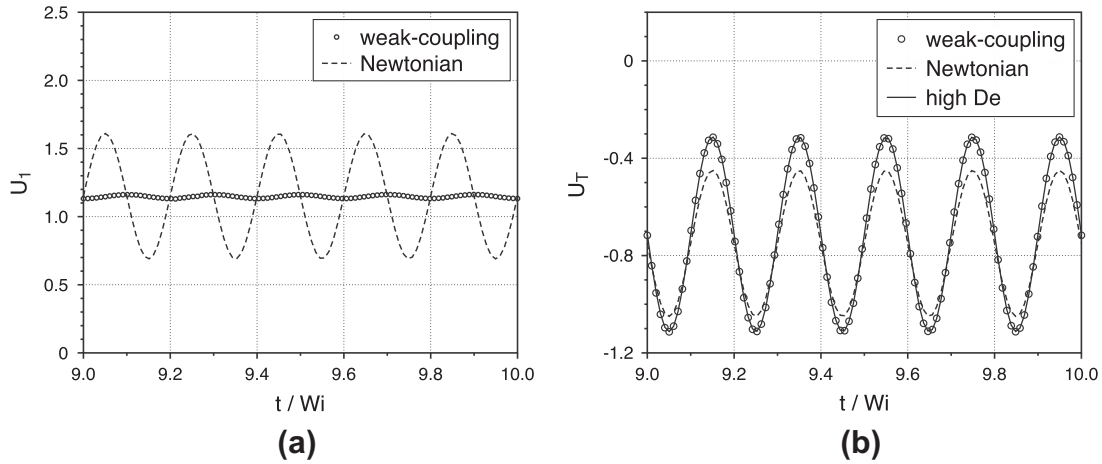


Fig. 10. (a) U_1 from an oscillatory flow with $A = 0.4$ computed by the weak-coupling method (open circles) with $Wi = 3$ and $De = 5$, along with the Newtonian response, $f(t)U_1^\infty(Wi)$ (dashed curve). (b) U_T with $\beta Wi = 0.25$, along with the prediction for a Newtonian fluid (dashed curve) and the high-Deborah-number prediction $U_T^{HD}(t)$ defined in the text (solid curve).

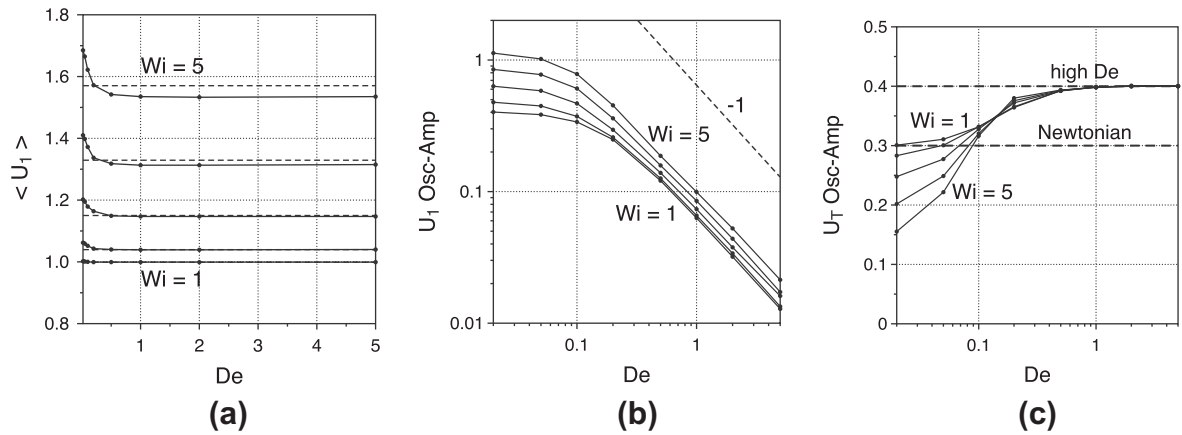


Fig. 11. (a) $\langle U_1 \rangle$ from the weak-coupling method (filled circles and solid curves) plotted against De , for $Wi = 1, 2, 3, 4, 5$ sweeping from bottom to top. Also shown is U_1^∞ for each Wi (dashed lines). (b) The oscillation-amplitude of U_1 plotted against De for the same set of Wi along with a power-law of De^{-1} . (c) The oscillation-amplitude of U_T plotted against De for the same set of Wi with $\beta Wi = 0.25$, along with the predictions for a Newtonian fluid and the high-Deborah-number model (labeled dashed lines). In all figures $A = 0.4$.

with U_0 . Fig. 11c shows that the amplitude of oscillation in U_T monotonically increases with De , but for larger Wi the transition becomes sharper and all curves appear to intersect at around $De = 0.14$. As seen in the figure, the amplitude of oscillation in U_T varies by up to a factor of 2.5 with De , making it a much more pronounced effect than any observed variations in the average velocity. The high-Deborah model predicts the amplitude to be enhanced by a factor of roughly βWi when compared to the Newtonian case, and this is confirmed for all of the cases tested. Intuitively, these exaggerated oscillations can be attributed to the intrinsic ‘springiness’ of the fluid – an effect that manifests in the regime of large De .

The observation of exaggerated motion about the mean for moderate to large Deborah numbers is in qualitative agreement with preliminary experiments to be reported separately. The experiments have also demonstrated little to no dependence of the mean velocity on the frequency of oscillation, in qualitative agreement with the findings here. This weak dependence is likely due to the geometric symmetry of the sphere as well as the symmetry of the forcing oscillation, and we speculate that stronger modifications of the mean speed might be observed if either of these symmetries are broken. This merits further investigation.

6. Discussion

The primary result of this paper is the exploitation of the weak-coupling limit for semi-analytical computations of viscoelastic flows. We have applied the expansion method to the classical problem of a sphere settling through a viscoelastic fluid, and have recovered previously observed behavior as well as presented new predictions for larger Wi . We have extended this classical problem to include time-dependent forcing and shown how the body’s motion is modified, with the most notable effect being exaggerated oscillations occurring for De order one and larger. Another result, more specific to the settling sphere problem, is the formal series solution which when truncated provides either a low- Wi or short-time asymptotic series (see Appendix B). This generalizes the low- Wi result of Leslie and Tanner for the Oldroyd-B model [5].

The advantages of the weak-coupling formulation are substantial, in both computational efficiency and stability, and we expect these advantages to transfer to other viscoelastic-fluid/structure problems. A natural application is many-bodied problems which may be made more computationally feasible by use of the weak-coupling formulation. We point out that many applications necessitate a spectrum of relaxation times to accurately model realistic

fluids, and this is a trivial extension of the results presented here. The only modification is that a set of polymeric stress fields evolve with the background flow, each of which contributes to the corrected body motion. Additionally, it is often advantageous to use more complex constitutive models, such as the FENE-type models, and the weak-coupling methodology can be applied to these models as long as there is no diffusion of the polymeric stress.

Several questions remain unanswered, even for the classical problem of a settling sphere. While we have determined the evolution of σ_0^p along the rear stagnation stream-line, a more complete treatment would determine the strand-width scaling, say through an analysis of higher spatial derivatives. We comment that our measurements of the strand width, along with the asymptotic scaling $\sigma_0^p \sim Wi^4$, gives an estimate of $\nabla \sigma_0^p$ that grows as $Wi^{4.8}$ within the strand. This rapid growth-rate may account for apparent singular behavior seen in many numerical simulations. Another interesting question is whether a retarded or a negative wake occurs behind the sphere within the weak-coupling limit for various constitutive models (see [29,30] for example), and what effect this has on the body's motion. This would require the computation of the return flow \mathbf{u}_1 , which is not a completely trivial numerical problem.

A promising future extension of this work is applying the weak-coupling expansion to the direct calculation of FENE kinetic models through the Smoluchowski equation. Often a closure approximation is used to reduce a kinetic model to a macroscopic model, for example in the FENE-P and FENE-CR models, but it is difficult to assess the effects of such approximations from a rigorous perspective and a direct computation of the true kinetic model is often desirable (see for example [31–33]). Consider a probability distribution of the polymer configuration $\Psi(\mathbf{X}, \mathbf{R}, t)$, where \mathbf{X} is the center of mass of a polymer and \mathbf{R} is the end-to-end vector. The distribution Ψ , along with a given, non-linear spring force law $\hat{\mathbf{F}}(\mathbf{R})$, together determine the macroscopic polymeric stress through a Kirkwood formula (see for example [34]). The evolution of Ψ is governed by the Smoluchowski equation

$$\partial_t \Psi + \mathbf{u} \cdot \nabla_{\mathbf{X}} \Psi + \nabla_{\mathbf{R}} \cdot (\dot{\mathbf{R}} \Psi) = 0, \quad (25)$$

where $\dot{\mathbf{R}} \equiv D\mathbf{R}/Dt$ depends functionally on $\nabla \mathbf{u}$, $\hat{\mathbf{F}}(\mathbf{R})$, and Ψ . Just as the weak-coupling expansion removes the \mathbf{X} -dependence in the Oldroyd-B partial differential equations, thereby reducing the system to a set of independent ODEs, here it removes the \mathbf{X} -dependence in the Smoluchowski equation and reduces it to a set of independent PDEs in \mathbf{R} and t . This is still a demanding computational problem, as a three-dimensional PDE must be evolved at every Lagrangian point, however removing the spatial-coupling makes it more amenable to parallel computation as compared to a formulation that is fully coupled.

Acknowledgments

We would like to thank Paulo Arratia, Eric Keaveny, Nathan Keim, Bin Liu, Trush Majmudar, and Jun Zhang for helpful discussions. This work was partially supported by NFS (DMS-0652775), DOE (DE-FG02-88ER25053), the MRSEC Program of NSF (DMR-0820341), and the Air Force (FA9550-10-1-018).

Appendix A. Exact solutions for Stokes flow past a sphere and the polymeric stress on the sphere-surface

The solution to Eqs. (9)–(11) is well-known Stokes flow past a sphere (see for example [35] pp. 121). Here we use a stream-function ψ in spherical coordinates. The components of \mathbf{u}_0 are denoted by u_r and u_θ .

$$\psi = \frac{1}{4} \sin^2 \theta (2r^2 - 3r + r^{-1}), \quad (A.1)$$

$$u_r = \frac{1}{r^2 \sin \theta} \partial_\theta \psi = \frac{1}{2} \cos \theta (2 - 3r^{-1} + r^{-3}), \quad (A.2)$$

$$u_\theta = -\frac{1}{r \sin \theta} \partial_r \psi = -\frac{1}{4} \sin \theta (4 - 3r^{-1} - r^{-3}). \quad (A.3)$$

The non-vanishing components of $\nabla \mathbf{u}_0$ in spherical coordinates are

$$L_{11} = \partial_r u_r = \frac{3}{2} \cos \theta (r^{-2} - r^{-4}), \quad (A.4)$$

$$L_{21} = \partial_r u_\theta = -\frac{3}{4} \sin \theta (r^{-2} + r^{-4}), \quad (A.5)$$

$$L_{12} = r^{-1} (\partial_\theta u_r - u_\theta) = \frac{3}{4} \sin \theta (r^{-2} - r^{-4}), \quad (A.6)$$

$$L_{22} = r^{-1} (\partial_\theta u_\theta + u_r) = -\frac{3}{4} \cos \theta (r^{-2} - r^{-4}), \quad (A.7)$$

$$L_{33} = r^{-1} (u_r + u_\theta \cot \theta) = -\frac{3}{4} \cos \theta (r^{-2} - r^{-4}). \quad (A.8)$$

Note that the basis vectors $\mathbf{e}_r, \mathbf{e}_\theta, \mathbf{e}_\phi$ associated with a given Lagrangian point $\mathbf{X}(\alpha, t)$ depend on time. When using the above equations in the weak-coupling Lagrangian method, we transform to a fixed basis to avoid introducing new terms into Eq. (16).

On the sphere-surface all entries of $\nabla \mathbf{u}_0$ vanish except for $L_{21} = \partial_r u_\theta$. Solving Eq. (16) gives $F_{11} = F_{22} = F_{33} = 1, F_{12} = 0$ and $F_{21} = -3/2 \tan \theta$. Let the components of σ_0^p be denoted by σ_{ij} . Evaluation of Eq. (17) gives

$$\sigma_{11} = 1, \quad (A.9)$$

$$\sigma_{12} = -\frac{3}{2} Wi \sin \theta (1 - e^{-t/Wi}), \quad (A.10)$$

$$\sigma_{22} = 1 + \frac{9}{2} Wi^2 \sin^2 \theta (1 - (1 + t/Wi) e^{-t/Wi}), \quad (A.11)$$

$$\sigma_{33} = 1. \quad (A.12)$$

On the sphere surface, Eq. (20) gives $\Phi = \sin^2 \theta (1 - e^{-t/Wi})$.

Appendix B. Series solution for the polymeric stress and the velocity correction

Here we find formal series solutions to Eqs. (17) and (19). Letting $\eta = t/Wi$, Eq. (12) in the Eulerian frame is

$$\partial_\eta \sigma_0^p + \sigma_0^p = \mathbf{I} - Wi(\mathbf{u} \cdot \nabla) \sigma_0^p + Wi(\nabla \mathbf{u}_0 \sigma_0^p + \sigma_0^p \nabla \mathbf{u}_0^T). \quad (B.1)$$

This equation is analytic in the variables η and Wi . We expand in Wi ,

$$\sigma_0^p(\mathbf{X}, \eta, Wi) = \sum_{n=0}^{\infty} Wi^n \Sigma_n(\mathbf{X}, \eta). \quad (B.2)$$

Consider the steady-state stress tensor $\Sigma_n^\infty(\mathbf{X}) = \lim_{\eta \rightarrow \infty} \Sigma_n(\mathbf{X}, \eta)$. This gives the iterative relationship

$$\Sigma_{n+1}^\infty = -(\mathbf{u}_0 \cdot \nabla) \Sigma_n^\infty + \nabla \mathbf{u}_0 \Sigma_n^\infty + \Sigma_n^\infty \nabla \mathbf{u}_0^T, \quad (B.3)$$

$$\Sigma_0^\infty = \mathbf{I}. \quad (B.4)$$

The time dependence can be determined in closed form as

$$\Sigma_n(\mathbf{X}, t/Wi) = f_n(t/Wi) \Sigma_n^\infty(\mathbf{X}), \quad (B.5)$$

$$f_n(t/Wi) = 1 - e^{-t/Wi} \sum_{k=0}^{n-1} \frac{(t/Wi)^k}{k!}. \quad (B.6)$$

We leave the analysis of the radius of convergence of series (B.2) for future work.

Now consider Φ defined in Eq. (20), and let

$$\Phi_n(\mathbf{X}, \eta) = \frac{4}{9} \nabla \mathbf{u}_0 : \Sigma_n(\mathbf{X}, \eta). \quad (B.7)$$

This implies

$$\Phi(\mathbf{X}, \eta, Wi) = \sum_{n=0}^{\infty} Wi^{n-1} \Phi_n(\mathbf{X}, \eta). \quad (\text{B.8})$$

As before, let $\Phi_n^\infty = \lim_{\eta \rightarrow \infty} \Phi_n(\mathbf{X}, \eta)$. Since the flow is incompressible, the trace of $\nabla \mathbf{u}_0$ vanishes and therefore Φ_0 vanishes. At first order, Eq. (B.3) shows that $\Sigma_1^\infty = \nabla \mathbf{u}_0 + \nabla \mathbf{u}_0^T$, and therefore Φ_1^∞ is a (normalized) dissipation rate, $\Phi_1^\infty = (4/9) \nabla \mathbf{u}_0 : (\nabla \mathbf{u}_0 + \nabla \mathbf{u}_0^T)$. Inserting the time-dependence gives

$$\Phi_1 = \frac{4}{9} \nabla \mathbf{u}_0 : (\nabla \mathbf{u}_0 + \nabla \mathbf{u}_0^T) (1 - e^{-t/Wi}) \quad (\text{B.9})$$

Beginning at second order, terms of the form $-(\mathbf{u}_0 \cdot \nabla) \Sigma_n^\infty$ enter in Eq. (B.3) and so analytic expressions become less convenient, however useful symmetry arguments can be made.

If n is even, the diagonal components of Σ_n are for-aft symmetric (i.e. symmetric with respect to θ about $\theta = \pi/2$) and the off-diagonal components are for-aft antisymmetric. If n is odd, then the diagonal is for-aft antisymmetric and the off-diagonal is for-aft symmetric. This can be shown through induction on n in Eq. (B.3). Additionally, $\nabla \mathbf{u}_0$ is for-aft antisymmetric on its diagonal and symmetric on its off-diagonal. When the contraction is taken in Eq. (B.7), Φ_n is for-aft symmetric when n is odd and antisymmetric when n is even. From Eq. (19), U_1 is related to Φ by the integration

$$U_1 = \frac{3}{4} \int_1^\infty r^2 dr \int_0^\pi \sin \theta d\theta \Phi(r, \theta). \quad (\text{B.10})$$

By the for-aft symmetry properties, the integral of Φ_n vanishes when n is even. Therefore, U_1 can be expressed as a summation of the odd terms only

$$U_1 = \sum_{n=0}^{\infty} Wi^{2n} a_{2n+1} f_{2n+1}(t/Wi), \quad (\text{B.11})$$

$$a_n = \frac{3}{4} \int_1^\infty r^2 dr \int_0^\pi \sin \theta d\theta \Phi_n^\infty(r, \theta). \quad (\text{B.12})$$

The $n-1$ derivatives of f_n vanish at zero, and therefore $f_n(t/Wi) \gg f_{n+1}(t/Wi)$ for $t/Wi \ll 1$. Thus the truncation of series (B.11), in addition to providing a low- Wi asymptotic series, provides a short-time asymptotic series. We note that linear short-time asymptotics can be computed for the full non-linearly coupled Stokes OB system, Eqs. (1)–(4), without appealing to the weak-coupling limit. This gives $U = 1 - \beta t + O(t^2)$, which is in agreement with the small t linearization of series (B.11).

In order to evaluate the series (B.11), we compute Σ_n iteratively through Eq. (B.3) with the aide of a symbolic program, and then evaluate Eqs. (B.7) and (B.12). The first few coefficients are

$$a_1 = 1, \quad (\text{B.13})$$

$$a_3 \approx -1.03 \times 10^{-2}, \quad (\text{B.14})$$

$$a_5 \approx 1.39 \times 10^{-2}, \quad (\text{B.15})$$

$$a_7 \approx -7.48 \times 10^{-3}, \quad (\text{B.16})$$

$$a_9 \approx 5.84 \times 10^{-3}, \quad (\text{B.17})$$

$$a_{11} \approx -6.16 \times 10^{-3}, \quad (\text{B.18})$$

$$a_{13} \approx 8.20 \times 10^{-3}. \quad (\text{B.19})$$

The coefficient a_3 agrees with that found by Leslie and Tanner, who determined the first two corrections in a steady-state, low- Wi expansion for the more general Oldroyd 6-constant model [5]. For the special case of Oldroyd-B, the advantages of the present calculation are that it can be taken out to arbitrary order and it provides dynamic information.

Inspection of the first few coefficients a_n suggests that the series is alternating and that the coefficients do not decay rapidly, if at all. This suggests the possibility of a finite radius of convergence and

singular behavior at a critical Weissenberg number (and possibly a critical time). In Section 4.1 we showed that σ_0^* is bounded in time for any Wi , however it is possible that higher spatial derivatives become singular. We leave this analysis for future-work, and simply note here that we have seen no indications of singular behavior arising from the weak-coupling numerical method.

References

- [1] W. Jones, A. Price, K. Walters, The motion of a sphere falling under gravity in a constant-viscosity elastic liquid, *Journal of Non-Newtonian Fluid Mechanics* 53 (1994) 175–196.
- [2] L. Becker, G. McKinley, H. Rasmussen, O. Hassager, The unsteady motion of a sphere in a viscoelastic fluid, *Journal of Rheology* 38 (1994) 377–403.
- [3] M. Arigo, D. Rajagopalan, N. Shapley, G. McKinley, The sedimentation of a sphere through an elastic fluid. Part 1. Steady motion, *Journal of Non-Newtonian Fluid Mechanics* 60 (1995) 225–257.
- [4] D. Rajagopalan, M. Arigo, G. McKinley, The sedimentation of a sphere through an elastic fluid part 2. Transient motion, *Journal of Non-Newtonian Fluid Mechanics* 65 (1996) 17–46.
- [5] F. Leslie, R. Tanner, The slow flow of a visco-elastic liquid past a sphere, *The Quarterly Journal of Mechanics and Applied Mathematics* 14 (1961) 36.
- [6] M. King, N. Waters, The unsteady motion of a sphere in an elasto-viscous liquid, *Journal of Physics D: Applied Physics* 5 (1972) 141.
- [7] B. Caswell, W. Schwarz, The creeping motion of a non-Newtonian fluid past a sphere, *Journal of Fluid Mechanics* 13 (1962) 417–426.
- [8] D. Joseph, J. Feng, The negative wake in a second-order fluid, *Journal of Non-Newtonian Fluid Mechanics* 57 (1995) 313–320.
- [9] K. Housiadas, R. Tanner, Perturbation solution for the viscoelastic 3D flow around a rigid sphere subject to simple shear, *Physics of Fluids* 23 (2011) 083101.
- [10] O. Harlen, J. Rallison, M. Chilcott, High-Deborah-number flows of dilute polymer solutions, *Journal of Non-Newtonian Fluid Mechanics* 34 (1990) 319–349.
- [11] O. Harlen, High-Deborah-number flow of a dilute polymer solution past a sphere falling along the axis of a cylindrical tube, *Journal of Non-Newtonian Fluid Mechanics* 37 (1990) 157–173.
- [12] C. Bodart, M. Crochet, The time-dependent flow of a viscoelastic fluid around a sphere, *Journal of Non-Newtonian Fluid Mechanics* 54 (1994) 303–329.
- [13] Y. Fan, Limiting behavior of the solutions of a falling sphere in a tube filled with viscoelastic fluids, *Journal of Non-Newtonian Fluid Mechanics* 110 (2003) 77–102.
- [14] J. Satrape, M. Crochet, Numerical simulation of the motion of a sphere in a Boger fluid, *Journal of Non-Newtonian Fluid Mechanics* 55 (1994) 91–111.
- [15] M. Renardy, Asymptotic structure of the stress field in flow past a cylinder at high Weissenberg number, *Journal of Non-Newtonian Fluid Mechanics* 90 (2000) 13–23.
- [16] P. Wapperom, M. Renardy, Numerical prediction of the boundary layers in the flow around a cylinder using a fixed velocity field, *Journal of Non-Newtonian Fluid Mechanics* 125 (2005) 35–48.
- [17] M. Renardy, A comment on smoothness of viscoelastic stresses, *Journal of Non-Newtonian Fluid Mechanics* 138 (2006) 204–205.
- [18] P. Becherer, A. Morozov, W. Saarloos, Scaling of singular structures in extensional flow of dilute polymer solutions, *Journal of Non-Newtonian Fluid Mechanics* 153 (2008) 183–190.
- [19] P. Becherer, W. Saarloos, A. Morozov, Stress singularities and the formation of birefringent strands in stagnation flows of dilute polymer solutions, *Journal of Non-Newtonian Fluid Mechanics* 157 (2009) 126–132.
- [20] R. Van Gorder, K. Vajravelu, F. Akyildiz, Viscoelastic stresses in the stagnation flow of a dilute polymer solution, *Journal of Non-Newtonian Fluid Mechanics* 161 (2009) 94–100.
- [21] R. Cressely, R. Hocquart, O. Scrivener, Birefringence d'écoulement localisée dans un dispositif à deux rouleaux, *Journal of Modern Optics* 25 (1978) 559–571.
- [22] O. Harlen, E. Hinch, J. Rallison, Birefringent pipes: the steady flow of a dilute polymer solution near a stagnation point, *Journal of Non-Newtonian Fluid Mechanics* 44 (1992) 229–265.
- [23] B. Thomases, M. Shelley, Emergence of singular structures in Oldroyd-B fluids, *Physics of Fluids* 19 (2007) 103103.
- [24] G. McKinley, R. Brown, Report of the VIIIth international workshop on numerical methods in viscoelastic flows, *Journal of Non-Newtonian Fluid Mechanics* 52 (1994) 407.
- [25] E. Lauga, Propulsion in a viscoelastic fluid, *Physics of Fluids* 19 (2007) 083104.
- [26] J. Teran, L. Fauci, M. Shelley, Viscoelastic fluid response can increase the speed and efficiency of a free swimmer, *Physical Review Letters* 104 (2010) 38101.
- [27] X. Shen, P. Arratia, Undulatory swimming in viscoelastic fluids, *Physical Review Letters* 106 (2011) 208101.
- [28] B. Liu, T. Powers, K. Breuer, Force-free swimming of a model helical flagellum in viscoelastic fluids, *Proceedings of the National Academy of Sciences* 108 (2011) 19516–19520.
- [29] O. Hassager, Negative wake behind bubbles in non-Newtonian liquids, *Nature* 279 (1979) 402–403.

- [30] O. Harlen, The negative wake behind a sphere sedimenting through a viscoelastic fluid, *Journal of Non-Newtonian Fluid Mechanics* 108 (2002) 411–430.
- [31] P. Halin, G. Lielens, R. Keunings, V. Legat, The Lagrangian particle method for macroscopic and micro–macro viscoelastic flow computations, *Journal of Non-Newtonian Fluid Mechanics* 79 (1998) 387–403.
- [32] P. Wapperom, R. Keunings, V. Legat, The backward-tracking Lagrangian particle method for transient viscoelastic flows, *Journal of Non-Newtonian Fluid Mechanics* 91 (2000) 273–295.
- [33] R. Keunings, Micro–macro methods for the multiscale simulation of viscoelastic flow using molecular models of kinetic theory, *Rheology Reviews* (2004) 67–98.
- [34] M. Doi, S. Edwards, *The Theory of Polymer Dynamics*, vol.73, Oxford University Press, USA, 1988.
- [35] J. Happel, H. Brenner, *Low Reynolds Number Hydrodynamics: With Special Applications to Particulate Media*, vol.1, Springer, 1983.